scientific reports

Check for updates

OPEN

Characterization of prostate macrophage heterogeneity, foam cell markers, and CXCL17 upregulation in a mouse model of steroid hormone imbalance

Samara V. Silver[1,2], Kayah J. Tucker[1,2], Renee E. Vickman[3], Nadia A. Lanman[4,5], O. John Semmes[1,2], Nehemiah S. Alvarez[6] & Petra Popovics[1,2]✉

Benign prostatic hyperplasia (BPH) is a prevalent age-related condition often characterized by debilitating urinary symptoms. Its etiology is believed to stem from hormonal imbalance, particularly an elevated estradiol-to-testosterone ratio and chronic inflammation. Our previous studies using a mouse steroid hormone imbalance model identified a specific increase in macrophages that migrated and accumulated in the prostate lumen where they differentiated into lipid-laden foam cells in mice implanted with testosterone and estradiol pellets, but not in sham animals. The current study focused on further characterizing the cellular heterogeneity of the prostate in this model as well as identifying the specific transcriptomic signature of the recruited foam cells. Moreover, we aimed to identify epithelia-derived signals that drive macrophage infiltration and luminal translocation. Male C57BL/6J mice were implanted with slow-release testosterone and estradiol pellets (T + E2) or sham surgery was performed and the ventral prostates were harvested two weeks later for scRNA-seq analysis. We identified *Ear2* + and *Cd72* + macrophages that were elevated in response to steroid hormone imbalance, whereas a *Mrc1* + resident macrophage population did not change. In addition, an *Spp1* + foam cell cluster was almost exclusively found in T + E2 mice. Further markers of foam cells were also identified, including *Gpnmb* and *Trem2*, and GPNMB was confirmed as a novel histological marker with immunohistochemistry. Foam cells were also shown to express known pathological factors *Vegf*, *Tgfb1*, *Ccl6*, *Cxcl16* and *Mmp12*. Intriguingly, a screen for chemokines identified the upregulation of epithelia-derived *Cxcl17*, a known monocyte attractant, in T + E2 prostates suggesting that it might be responsible for the elevated macrophage number as well as their translocation to the lumen. Our study identified macrophage subsets that responded to steroid hormone imbalance as well as further confirmed a potential pathological role of luminal foam cells in the prostate. These results underscore a potential pathological role of the identified prostate foam cells and suggests CXCL17-mediated macrophage migration as a critical initiating event.

Keywords Benign prostatic hyperplasia, Cytokines, Lower urinary tract symptoms, Foam cells

Benign Prostatic Hyperplasia (BPH) is a complex pathological disorder in the prostate mainly characterized by the formation of non-malignant nodules in the transition zone[1,2]. The prevalence of BPH progressively increases with age affecting 70% of men in their 60 s[3]. Among men aged 50 years and older, BPH is the fifth most common non-malignant disease and represents a significant economic burden in the US[4]. BPH instigates a range of urinary problems, such as voiding and irritative symptoms, collectively known as lower urinary tract symptoms (LUTS),

[1]Department of Microbiology and Molecular Cell Biology, Eastern Virginia Medical School, Norfolk, VA 23507, USA. [2]Leroy T. Canoles Jr. Cancer Research Center, Eastern Virginia Medical School, Norfolk, VA, USA. [3]Department of Surgery, Endeavor Health, An Academic Affiliate of the University of Chicago Pritzker School of Medicine, Evanston, IL, USA. [4]Institute for Cancer Research, Purdue University, West Lafayette, IN, USA. [5]Department of Comparative Pathobiology, Purdue University, West Lafayette, IN, USA. [6]Department of Physiological Sciences, Eastern Virginia Medical School, Norfolk, VA, USA. ✉email: PopoviP@evms.edu

which can significantly diminish the quality of life[5]. LUTS/BPH is also linked to a range of complications, including but not limited to urinary tract infection, acute urinary retention, urolithiasis, and renal failure[6]. Meanwhile, current medical modalities targeting smooth muscle dysfunction via alpha-blockers and proliferation via 5-alpha reductase inhibitors often fail[7], suggesting that other prostate pathologies play important roles in BPH etiology.

Inflammation and fibrosis are two interconnected processes proposed to drive BPH progression and symptomology. Chronic inflammation is associated with BPH, particularly as the size of the prostate increases, characterized by the dominance of T lymphocytes and macrophages[8,9]. In turn, chronic inflammation drives fibrosis leading to the worsening of urinary issues due to an impact of urethral resistance[10,11]. Chronic inflammation, fibrosis, as well as proliferation in the prostate is instigated by various factors, including epithelial and fibroblast senescence and related secretion of cytokines, chemokines (IL-8, CXCL12, IL-1α) and growth factors (FGF-2, FGF-7)[12–14], western diet and associated metabolic syndrome[15] as well as the increasing dominance of estradiol with aging[16,17]. To further decipher the role of the latter factor, our group has previously utilized a mouse model of steroid hormone imbalance that is created by the subcutaneous implantation of slow-release testosterone and estradiol pellets[18,19]. We found that macrophages were the primary type of immune cell to be significantly increased in this model after only two weeks, with the ventral prostate lobe experiencing the most substantial rise[19]. Most importantly, we identified that macrophages migrate to the lumen in both the mouse model and human BPH, take up lipids and adopt the foam cell phenotype[19]. However, their significance in BPH progression remains largely unclear.

The accumulation of foam cells in the arterial wall is a hallmark of early atherosclerotic lesions, known as fatty streaks[20]. Furthermore, foam cells undergo programmed cell death, leading to the formation of a necrotic core and inflammatory cell infiltration within the plaque, which is a key feature of advanced atherosclerotic lesions[20,21]. Foam cells have also been indicated to drive fibrosis in the lung[22]. These findings imply that foam cells will most likely promote inflammation and fibrosis in the prostate. In the steroid hormone imbalance model, fibrosis develops at a later stage (beyond 12 weeks)[19], potentially due to the persistence of foam cells.

To gain a deeper insight into the pathological impact of the shifting immune environment due to steroid hormone imbalance, we utilized single-cell RNA sequencing (scRNA-seq) on the ventral prostate lobe and examined alterations in cell clusters. We selected the ventral lobe, since this was the major location of foam cell formation and a 2-week timepoint, which is when urinary frequency starts to develop in this model[23]. This has identified a marked increase in progenitor and basal epithelial cells as well as revealed four distinct macrophage subsets, including an *Spp1* + foam cell cluster. Additionally, we identified the marker gene signatures and pathological factors exhibited by *Spp1* + macrophages, which will be crucial for future efforts to target these cells and determine their function. Finally, from the transcriptomic changes in resident prostate cells, we identified key cytokines/chemokines that are implicated in remodeling the immune environment.

Methods

Ethics statement

All experiments were conducted under approved protocols from the Eastern Virginia Medical School Animal Care and Use Committee (ID:22-011) and in accordance with the National Institutes of Health Guide for the Care and Use of Laboratory Animals. In addition, the authors complied with the ARRIVE guidelines.

Mice

C57BL/6J male mice were obtained from The Jackson Laboratory. Animals were maintained on a strict 12:12 h light–dark cycle in a temperature- and humidity-controlled facility with water and food provided ad libitum. Testosterone (25 mg) and estradiol mixed with cholesterol (2.5 mg and 22.5 mg, respectively) were compressed as pellets and were surgically implanted subcutaneously to 8-week-old mice, as previously[18,19]. Control mice underwent sham surgery and ventral prostate lobes were collected two weeks post-procedure. Experimental groups involved 8 mice (2/group for scRNA-seq and 6/group for histological tests). The actual count of data points may vary as a result of tissue loss or the removal of low-quality samples.

Cell dissociation, library preparation and sequencing

Paired ventral prostate lobes were collected into one tube for each animal in ice-cold PBS and were transferred to 100 µl of 10 mg/mL (in HBSS) *Bacillus licheniformis* protease (Creative Enzymes, Shirley, NY). Tissues were agitated at 6 °C at speeds ranging from 600 to 1000 rpm for up to one hour, with intermittent pipetting, until noticeable cell separation was observed. Cells were then passed through a 40 µm mesh strainer and cell viability was assessed on a Countess 3 FL and ranged between 72 and 78%. Following the guidelines from the Chromium Next GEM Single Cell manual, we determined the optimal cell loading to be 7000 cells per sample.

Cells were barcoded and libraries were generated for duplicate samples per group using the Chromium Next GEM Single Cell 3′ Kit v3.1. Libraries were created from each animal and concentrations were calculated based on Tapestation data (200–1000 bp). Samples were also quantified with Qubit before sequencing to balance the libraries. Paired-end sequencing was conducted on a NextSeq2000 instrument. Run metrics for scRNA-seq of sham and T + E2 mouse prostate samples were calculated by Cell Ranger v7.2.0 (Supplementary Table S1).

FASTQ files were aligned to *Mus musculus* GRCm39 (Ensembl release 111)[24] cDNA reference for all annotated RNA was prepared using kallisto (v0.46.1) and bustools (v0.39.4)[25]. Transcript counts were aggregated to gene counts using bustools. The count matrix was imported into R (v4.3.2, Bioconductor v3.18.1) and analyzed using Seurat package (v. 5.0.1)[26,27] and was filtered such that each cell had a minimum of 200 genes and those genes were detected in at least 3 cells. Cells were retained for further analysis if they contained less than 5% mitochondrial reads and 3000 reads/cell. The cold protease method of digestion may have resulted in low cell quality, so strict filtering for mitochondrial reads was included to limit analysis of stressed cells. Using Seurat,

data sets were integrated, normalized, scaled (linear model, no regression), and dimensionally reduced using 30 PCs, followed by UMAP to visualize clusters of cells using the top 3000 variable genes and a resolution of 0.8. A second unsupervised clustering was done for fibroblast clusters using the same strategy as above.

Differential gene expression analysis was conducted utilizing the FindMarkers function integrated within the Seurat package, employing the Wilcoxon Rank Sum test for statistical evaluation. Gene Ontology (GO) analysis of biological processes was performed using the clusterProfiler package and pathways with adjusted p values < 0.05 retained[28].

Immunohistochemistry

Sections were de-paraffinized and hydrated. Antigen retrieval was performed in a decloaking chamber (Biocare Medical, Pacheco, CA, USA) using citrate buffer pH 6.0. Endogenous peroxidases and non-specific binding sites were blocked with Bloxall (Vector Laboratories, Burlingame, CA, USA), rodent block (Biocare Medical) and horse serum (10%). Primary antibodies anti-NR2F6/Ear2 (ab137496, Abcam, Waltham, MA, USA, 1:3000 dilution), anti-GPNMB (ab188222, Abcam, Waltham, MA, USA, 1:1000 dilution) were added overnight. An HRP-conjugated horse anti-rabbit IgG Polymer (Vector Laboratories) was used as secondary for 30 min and the signal was developed using the SignalStain DAB Substrate Kit (Cell Signaling). For IF, anti-CD68 (ab283654, Abcam, Waltham, MA, USA, 1:1000 dilution) and anti-CD72 (AF1279, R&D Systems, Minneapolis, MN, USA, 1:40 dilution) antibodies were co-administered overnight and were labeled with horse anti-rabbit or anti-goat Dylight 488 and 594 (Vector Laboratories, 1:300 dilution) secondary antibodies for 30 min. Alternatively, an Opal kit (Akoya Biosciences, Marlborough, MA, USA) was used with anti-NR2F6/Ear2 (ab137496, Abcam, Waltham, MA, USA, 1:700 dilution) and anti-CD206/Mrc1 (24595T, Cell Signaling, Danvers, MA, USA, 1:500 dilution) primary antibodies.

In situ hybridization

In situ hybridization was performed with RNAscope using probe sets specific for *Ccl6, Cd209a, Col12a1, Cxcl13, Cxcl17, Fbn1, Vegfa,* and *Tgfb1* with the RNAscope® 2.5 HD Assay-Dual or -Brown detection system (Advanced Cell Diagnostics, Newark, CA, USA). Reaction specificity was tested with a positive control probe and a negative control with only a probe diluent instead of the probe.

Imaging and analysis

Tissues were imaged with a Mantra 2 Quantitative Pathology Workstation (Akoya Biosciences, Marlborough, MA, USA) with a 40 × objective. Six representative images were taken per tissue. Area not containing tissue and prostate lumens were removed to obtain total tissue area to normalize positive cell counts that were manually counted. Both experimental groups were represented on each tissue blocks/slides, and slides from the same tissue and timepoint were processed together.

Statistical analysis

Statistical tests were conducted in Graphpad Prism (Graphpad Software, ver: 9.4.1., San Diego, CA, USA). For histological analyses, we used two-tailed t-test when the F-test was significant. Otherwise, the statistical difference was determined by Mann–Whitney non-parametric test. P-values below 0.05 were accepted as significant. Error bars represent SEM.

Results

Cell cluster analysis showed an increase in basal and progenitor epithelial cells in T + E2 mice

Single cell libraries were generated for two prostates per experimental group (sham1, sham2, te2-1, te2-2). It is unclear why the sham control samples had fewer genes identified per cell, but may have been related to adjusting to a longer digestion time with cold protease due to the larger T + E2 ventral lobes. Following data filtering, retained cell counts were as follows: 1255 cells for sham1, 1105 for sham2, 1403 for te2-1, and 1031 for te2-2. Using the Seurat R package, data sets were integrated, scaled, and dimensional reduction was performed to find clusters of cells, and genes enriched within each cluster.

Nineteen clusters were first identified (Supplementary Fig. S1) from the integrated dataset containing all sham and te2 samples. Canonical lineage-defining markers expressed in the integrated dataset (based on shared genes across treatment groups) were used to annotate clusters (Supplementary Table S2). Three epithelial clusters deemed highly similar were merged (defined as EpiA cells). Two clusters of prostate basal cells were identified using *Krt5* and *Krt14* markers and subsequently combined. Three presumed epithelial clusters (clusters 7, 8, and 18) possessed an overall downregulation in epithelial marker expression potentially indicating low viability in these clusters and were therefore removed from further analysis. A total of five clusters showed marker gene *Krt8* and *Krt18* expression as signatures of luminal cells after the merges and the elimination of low-viability clusters (Fig. 1A,B, Supplementary Table S3). Basal epithelial cells were identified via *Cp*, *Pdgfa*, *Apoe* and *Col4a2* expression (Fig. 1B, Supplementary Table S3). EpiA cells were *Sbp*^{high} and *Spink1*^{high} and showed marked expression of *Crabp1* (Fig. 1B), and EpiB cells were identified via the expression of *Nkx3-1*, *Mmp7*, *Pbsn* and *Msmb*[29]. We also identified two epithelial clusters that had high expression of *Mki67* proliferation marker as well as cell cycle-associated genes *Cdca3, Ccnb2, Cdc6* and *Ccne2* (Fig. 1B), whereas top 10 gene ontology (GO) pathways of biological processes were associated with RNA processing and DNA replication (Fig. 1C), suggesting that these clusters consist mainly of proliferating luminal cells (ProlifEpi1 and 2). EpiProgenitor cells presented markers of the urothelial epithelial cell lineage identified by Joseph et al. and progenitor markers *Krt4*, *Krt7*, *Klf5* and *Slc39a8*[30]. These urothelial epithelial cells were previously identified as prostate luminal cells based on localization in proximal ducts[30]. Similar progenitor cells were identified by Guo et al. via markers *Tacstd2*, *Krt4*

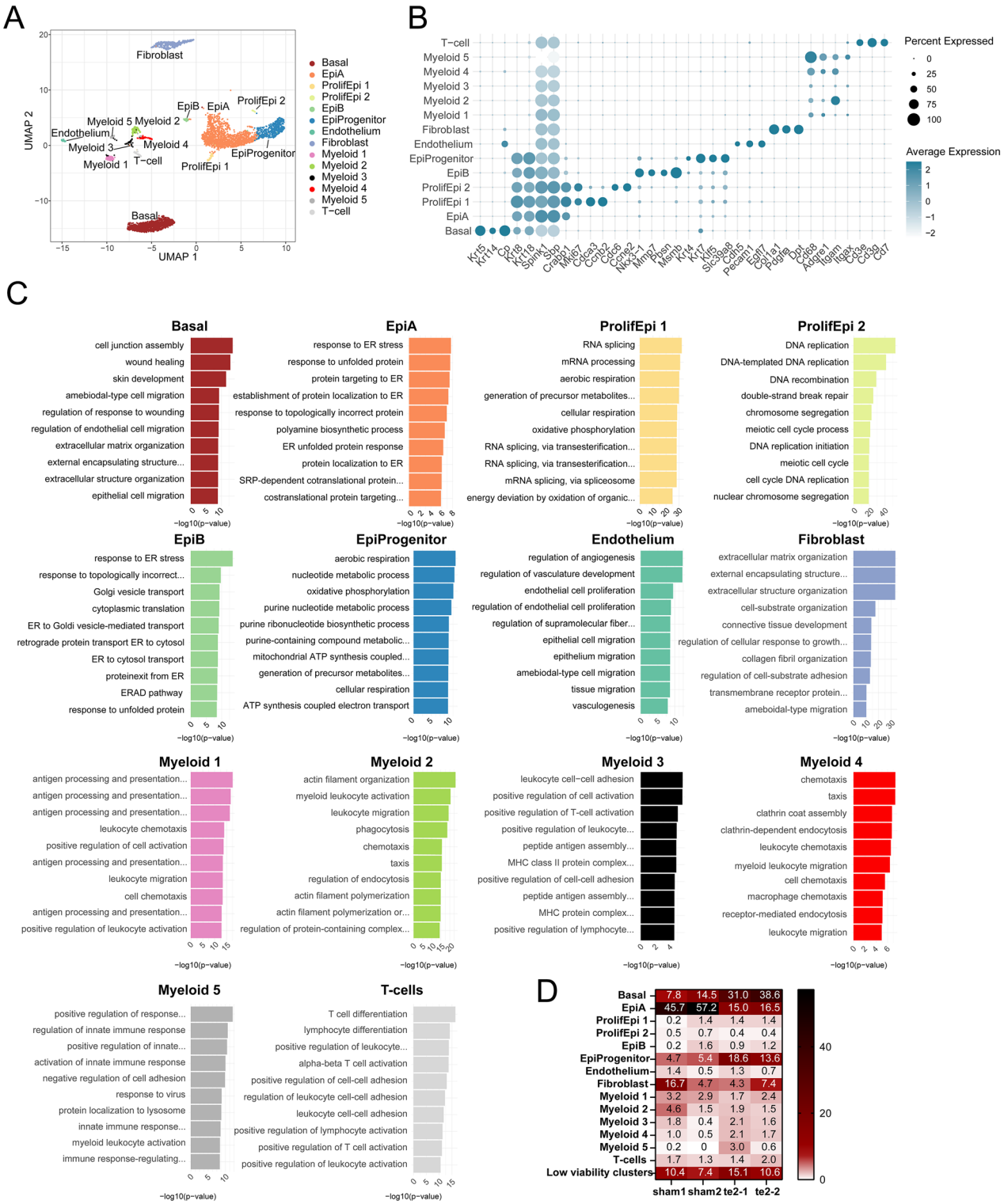

Fig. 1. Identification of mouse prostate cell types of sham and T + E2 mice using scRNA-seq. (**A**) Major cell lineage clusters based on Uniform Manifold Approximation and Projection (UMAP) embedding of jointly analyzed single-cell transcriptomes from ventral prostate lobes of two sham and two T + E2 mice. After merging highly similar clusters and removing low viability groups (Supp. Fig.), a total of 14 clusters were annotated. (**B**) Dot blot of selected gene markers used for cell-type identification. (**C**). Top 10 Gene Ontology terms for biological processes for each cluster. Pathways with adjusted p values < 0.05 were retained. (**D**) Distribution of cell types within samples shown as % of sample total.

and *Psca*[29] and by Crowley et al. via a common proximal marker, *Ppp1r1b*[31]. EpiProgenitor cells were enriched in metabolic pathways (Fig. 1C). A separate periurethral epithelial cluster that was identified by others via *Ly6d* and *Aqp3*[31] was not found in our dataset.

Endothelial cells exhibited positivity for *Cdh5*, *Pecam1* and *Egfl1* (Fig. 1B, Supplementary Table S3). Fibroblasts were delineated by the expression of *Col1a1*, *Pdgfra* and *Dpt*. Myeloid clusters were identified by the expression of *Cd68*, *Adgre1* (F4/80), *Itgam* and *Itgax*. T-cell identification was based on the expression of *Cd3e* and *Cd3g* and *Cd7*. Smooth muscle cell markers *Acta2* and *Tagln* are expressed in about 5% of cells or less in the fibroblast cluster suggesting that the majority of these cells have been lost during tissue dissociation (data not shown).

We then looked at the contribution of each sample to cell clusters. This analysis showed (Fig. 1D) that EpiA cells decreased whereas Basal cells and EpiProgenitor cells were markedly increased in T + E2 mice. In addition, Myeloid 5 cells were almost exclusively in T + E2 mice (2 cells in sham vs. 48 cells in te2). This showed a major rearrangement in cellular heterogeneity in the prostate in response to the two-week exposure to steroid hormone imbalance.

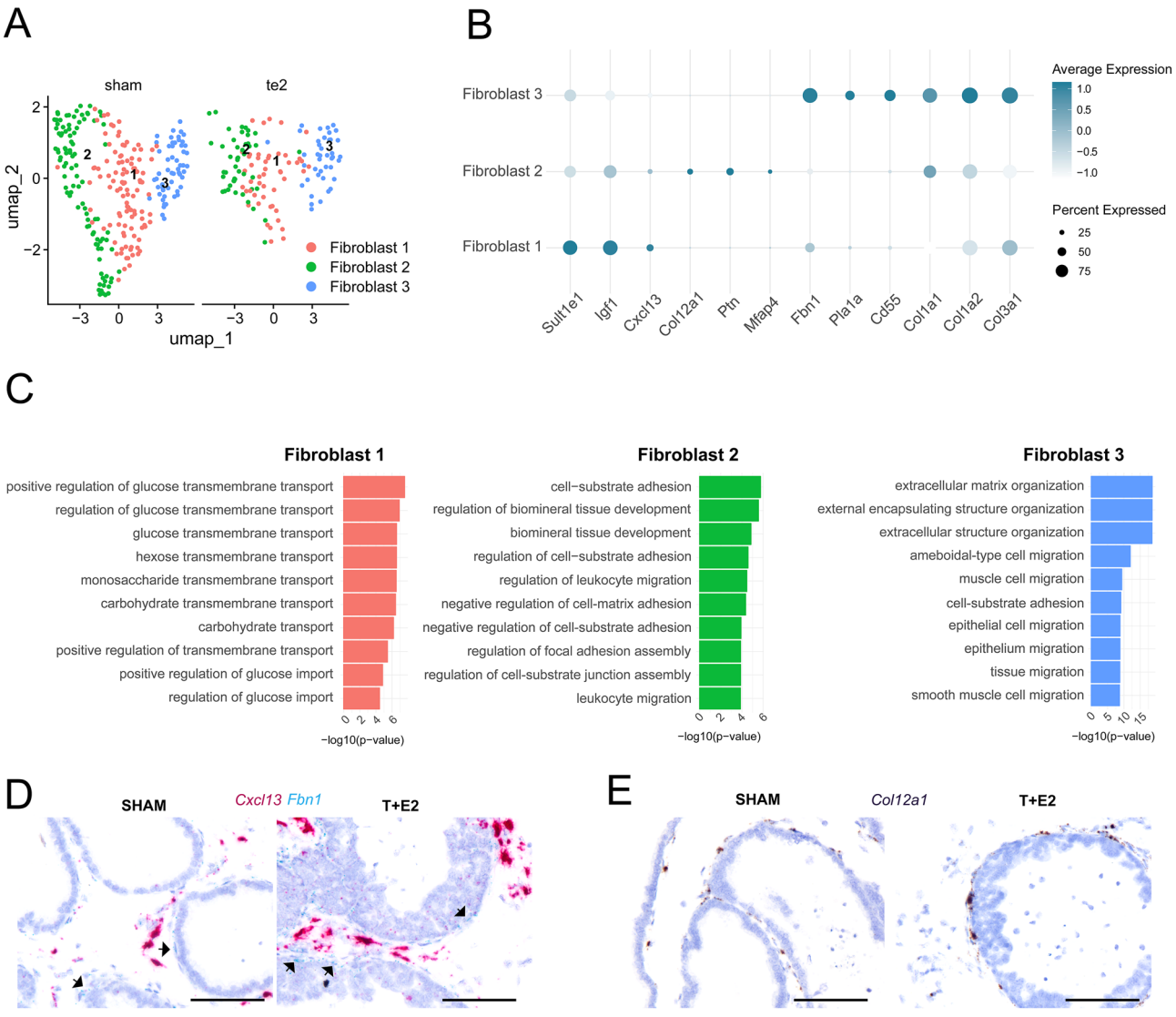

Fig. 2. Analysis of fibroblast cell clusters in sham and T + E2 ventral prostates. The fibroblast cluster was further divided by Uniform Manifold Approximation and Projection (UMAP) and RNAscope was used to confirm the spatial distribution of fibroblast subclusters. (**A**) Subclustering of the fibroblast cluster identified 3 fibroblast lineages. (**B**) Dot blot of markers differentiating the fibroblast clusters (*Sult1e1*–*Cd55*) and delineating extracellular matrix production (*Col1a1*, *Col1a2*, *Col3a1*). (**C**) Top 10 gene ontology terms for biological processes associated with fibroblast subclusters. Pathways with adjusted p values < 0.05 were retained. (**D**) Localization of Fibroblast 1 (*Cxcl13*$^{+}$) and Fibroblast 3 (*Fbn1*$^{+}$) cells via in situ hybridization. (E) Spatial distribution of Fibroblast 2 cells (*Col12a1*$^{+}$) via in situ hybridization. Scale bars represent 100 µm.

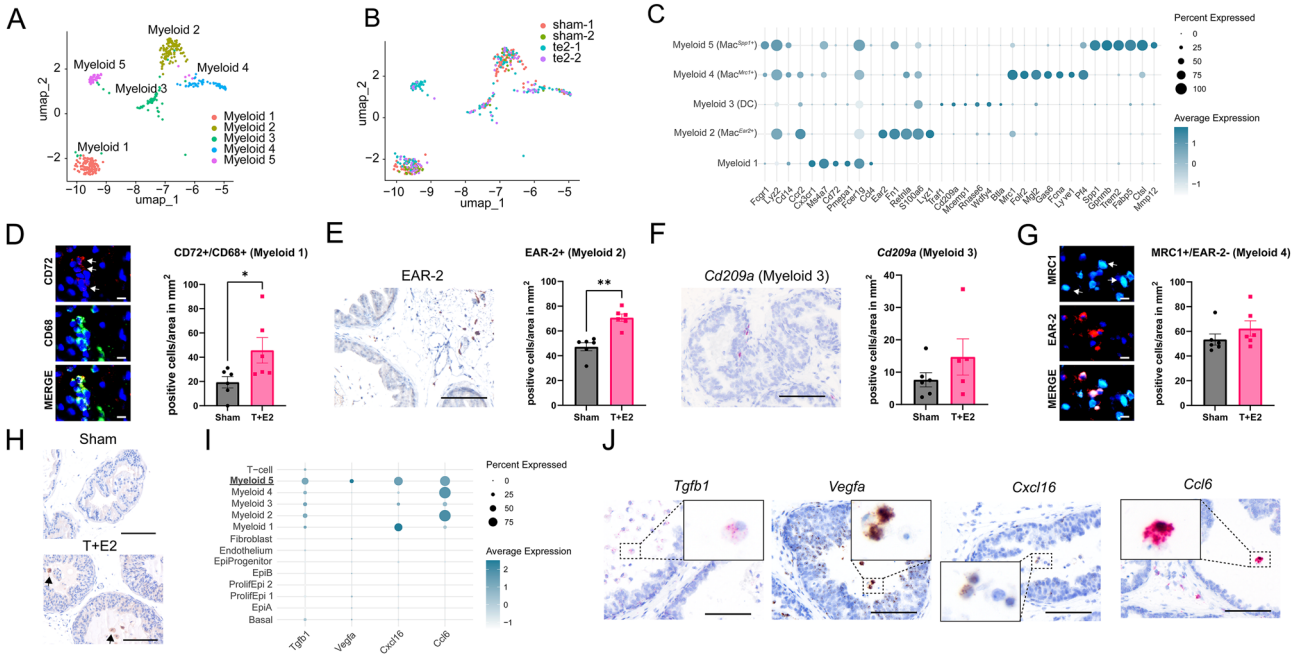

Fig. 3. Analysis of myeloid cluster markers and Mac^{Spp1+} pathological gene transcriptome. The scRNA-seq data for myeloid clusters was further analyzed to determine cluster markers which were then confirmed using immunohistochemistry and RNAscope methods. This Figure also reports on selected secreted factors of luminal macrophages and their confirmation with RNAscope. (**A**) Uniform manifold approximation and projection (UMAP) visualization of myeloid clusters. (**B**) Distribution of treatment groups across myeloid clusters. (**C**) Expression of known markers of macrophages/monocytes (*Fcgr1-Ccr2*) and our markers of Myeloid 1 (*Ms4a7-Ccl4*), 2 (*Ear2-S100a6*), 3 (*Traf1-Btla*), 4 (*Mrc1-Pf4*), and 5 (*Spp1-Mmp12*) clusters. (**D**) Representative image of CD72 + /CD68 + immunofluorescence (IF) to identify Myeloid 1 cells and quantification in Sham vs. T + E2. (**E**) Representative image of EAR-2 + immunohistochemistry (IHC) to identify Myeloid 2 cells and quantification in sham vs. T + E2. (**F**) Representative image of Cd209a mRNA via in situ hybridization to identify Myeloid 3/Dendritic cells and quantification in sham vs. T + E2. (**G**) Representative image of MRC1 + /EAR-2− IF to identify Myeloid 4 cells and quantification in sham vs. T + E2. (**H**) Representative image of GPNMB of Myeloid 5 luminal macrophages in sham and T + E2 tissue. (**I**) Further profibrotic, proinflammatory and pro-angioneic factors expressed in Mac^{Spp1+} macrophages. (**J**) Validation of mRNA expression of *Tgfb1* (red), *Vegfa* (brown), *Cxcl16* (brown), and *Ccl6* (red) in luminal macrophages via in situ hybridization. Only examples of T + E2 tissues are shown. Scale bars represent 100 µm except (**D**) and (**G**), where scale bars are 10 µm. Error bars represent SEM.

A subepithelial fibroblast cluster was the primary producer of collagens

The fibroblast cluster was further divided into three subclusters via a second unsupervised clustering (Fig. 2A). Marker genes of these fibroblast clusters were identified as *Sult1e1*, *Igf1* and *Cxcl13* for Fibroblast 1 *Col12a1*, *Ptn* and *Mfap4* for Fibroblast 2 and *Fbn1*, *Pla1a* and *Cd55* for Fibroblast 3 (Fig. 2B). The Fibroblast 1 cluster had similar gene signature to what has been identified as "Prostate fibroblast" by Joseph et al.[32], however marker genes of "urethral" (*Lgr5*, *Apoe, Osr1* and *Sfrp2*) and "ductal" fibroblast (*Wnt2, Rorb, Wif1, Ifitm1* and *Srd5a2*) were only present at very low levels (data not shown). Extracellular matrix markers of fibrosis, *Col1a1*, *Col1a2* and *Col3a1* were most pronounced in Fibroblast 3 cells (Fig. 2B). Several GO terms of biological processes associated with extracellular matrix production were also identified in this cluster (Fig. 2C). These cells might be the main matrix producers in the advanced stages of this mouse model[19]. Fibroblast 1 cells were linked to increased glucose uptake, whereas Fibroblast 2 cluster was associated with cell–matrix adhesion. Localization of fibroblasts was assessed by RNAscope using *Cxcl13* (Fibroblast 1, red), *Col12a1* (Fibroblast 2, brown) and *Fbn1* (Fibroblast 3, blue) and showed that Fibroblast 1 cells were primarily in the interstitial region whereas Fibroblast 2 and 3 cells were subepithelial (Fig. 2D,E). We quantified the expression of this markers in sham vs. T + E2 mice, but did not find significant changes (Supplementary Fig. S2), reiterating that fibrosis may develop at a later stage in this model.

Intraluminal tissue involution was composed of fibroblasts in T + E2 mice

Histological analysis also identified the presence of incidental intraluminal tissue invaginations that phenotypically resembled stromal nodules and seemed to be rooted in the subepithelial stroma. This was the first time, to the best of our knowledge, that these structures were described in this model. Calculations of tissue cell counts in our prior analyses excluded these areas. To understand the cell-composition of these structures, we re-assessed fibroblast markers *Col12a1*, *Cxcl13* and *Fbn1*, as well as E-cadherin epithelial marker in these structures. We

found that all three fibroblast markers were expressed in the invaginations (Supplementary Fig. S3), but not E-cadherin, further confirming the stromal composition of these invaginations. We believe that such structures may be useful in studying the origination of stromal nodules in the future.

Three macrophage clusters were increased in response to steroid hormone imbalance

Myeloid clusters were present in all samples, with the exception of the Myeloid 5 cluster, which was almost uniquely composed of cells from the T + E2 samples (Fig. 3A,B). Using a range of monocyte/macrophage markers based on[33] including *Fcgr1, Lyz2, Cd14, Ccr2 and Cx3cr1*, we delineated that clusters Myeloid 1, 2, 4 and 5 were most likely monocyte/macrophage subsets. Interestingly, Myeloid 1 cells expressed a higher level of *Cx3cr1* (Fig. 3C) and *Spn* (Supplementary Table S3) non-classical monocyte markers[34], whereas Myeloid 2 and 4 possessed elevated *Ccr2* levels representing classical monocytes[35] and suggesting that these clusters were composed of specific monocyte lineages and their macrophage derivatives. Genes enriched were *Ms4a7*, *Cd72, Pmepa1, Fcer1g and Ccl4* in the Myeloid 1 cluster, *Ear2*, *Fn1*, *Retnla*, *S100a6 and Lyz1* in the Myeloid 2 cluster and *Mrc1, Folr2*, *Mgl2*, *Gas6*, *Fcna*, *Lyve1* and Pf4 in Myeloid 4 cluster (Fig. 3C). The expression of *Folr2* and *Lyve1* suggest that Myeloid 4 cells were resident macrophages whereas *Retnla*, *Lyz1*, and *Ear2* expression identified the Myeloid 2 cluster as potentially alternatively activated (M2) macrophages[36,37]. The expression of *Ccl4* and *Cd74* pro-inflammatory markers, and an interferon response gene (*Irf8*) in Myeloid 1 cells (Supplementary Table S3) suggests a pro-inflammatory phenotype[38]. In agreement with this, the top GO terms associated with this cluster indicated cell activation and leukocyte chemotaxis (Fig. 1C). Myeloid 3 cells were marked by genes *Traf1*, *Cd209a*, *Mcemp1*, *Rnase6*, *Wdfy4* and *Btla* delineating these cells as dendritic cells (DCs) most likely derived from monocytes[36]. Top GO terms of biological processes in this cluster were related to antigen presentation (MHC complex, T-cell activation, Fig. 1C) in agreement with the proposed cell type function. Most intriguingly, Myeloid 5 cells contained uniquely high levels of *Spp1* (Mac^{Spp1+}, Fig. 3C, Supplementary Table S3). Our group has previously identified *Spp1* as a marker of lipid-laden luminal macrophages in the mouse ventral prostate otherwise known as foam cells. Examples of genes further distinguishing the Mac^{Spp1+} cluster were *Fabp5*, *Ctsl*, *Gpnmb*, *Mmp12* and *Trem2*, which markers were also predominant in foamy macrophages in mouse atherosclerotic lesions[39].

Myeloid 1 cells were labeled based on $CD72^{+}CD68^{+}$ dual positivity in the tissues and were shown to be increased by T + E2 treatment (Fig. 3D). The addition of the CD68 was required to exclude potential B-cells that are known to be positive for CD72. The EAR-2 positive Myeloid 2 (Mac^{Ear2+}) macrophages localized to the interstitial stroma and were increased by 50% in response to T + E2 treatment (Fig. 3E). DCs were localized in the periglandular area shown via Cd209a in situ hybridization, but were not significantly elevated in response to T + E2 treatment (Fig. 3F). Myeloid 4 cells were labelled using MRC1 (Mac^{Mrc1+}), however, a small subset of Mac^{Ear2+} were also expected to stain for this marker based on Fig. 3C. Therefore, we identified these cells based on MRC1 + EAR2− staining and found that they were localized in the stroma and around the epithelium and capillaries, but did not significantly change in number in response to treatment (Fig. 3G). Using immunohistochemistry, we confirmed that GPNMB protein expression was limited to luminal cells with foam cell morphology and were only detected in the T + E2 group (Fig. 3H).

Spp1 + macrophages expressed *Tgfb1*, *Mmp12*, *Cxcl16*, *Ccl6* and *Vegfa* potential pathological factors

To understand the functional role of the Mac^{Spp1} macrophages, we screened their transcriptome for genes that encode secreted proteins and therefore may influence nearby epithelial cells. Mac^{Spp1} marker genes with p value < 0.001 were loaded to a Uniprot batch analysis. This search identified 61 genes that encode secreted proteins (Supplementary Table S7). From these genes, we selected factors with previously identified pathological roles including *Transforming growth factor beta 1* (*Tgfb1*)[40,41], *Matrix metalloproteinase 12* (*Mmp12*)[42], *chemokine (c–c motif) ligand 6* (*Ccl6*)[43] and *Vascular endothelial growth factor-a* (*Vegfa*)[44] for further analysis via dot blot across cell clusters. We also included *Chemokine (c-x-c motif) ligand 16* (*Cxcl16*), which was primarily categorized as a transmembrane protein in the Uniprot database, but has been shown to be a soluble attractant for T-cells[45]. Dot blot analysis showed that *Cxcl16* was also expressed in Mac2 and *Ccl6* in Mac1 cells (Fig. 3I). We then confirmed the expression of these markers in luminal macrophages using RNAscope (Fig. 3J). *Vegfa* showed high expression in luminal macrophages and was also moderately elevated in epithelial cells (Fig. 4C). *Cxcl16*, *Tgfb1* and *Ccl6* also showed positive staining in luminal cells. In addition, Mac^{Spp1} cells in tissue had a foam cell phenotype with elevated intracellular lipid[19]. Thus, a panel of genes involved in lipid metabolism were evaluated. Mac^{Spp1} cells had marked increase in the expression of genes related to lipid uptake (*Cd36*)[46] intracellular trafficking (*Fabp4* and *Fabp5*)[47] and efflux (*Abcg1* and *Abca1*, Supplementary Fig. S4)[48].

Steroid hormone imbalance upregulated the monocyte attractant *Cxcl17* in epithelial cells

Our previous study[19], as well as the current analysis, highlighted that steroid hormone imbalance drove monocyte infiltration to the prostate as well as the translocation of macrophages to the prostate lumen where they differentiated into foam cells. In order to assess how resident prostate cells directed the remodeling of the immune environment, we visualized the cytokine expression profile across epithelial, fibroblast and endothelial clusters in T + E2 treated versus control cells (Fig. 4). Differential expression (DE) analysis was completed and statistical analysis was performed using non-parametric Wilcoxon Rank Sum test (Supplementary Table S6). A screen through all interleukins (ILs) identified *Il33* as being predominantly upregulated in basal epithelial cells and fibroblasts ($p < 0.001$, Fig. 4A) and induced by T + E2 treatment (Fig. 4B). *Il33* is a nuclear cytokine and only activates immunological response upon cell damage and extracellular release[49]. We also screened chemokine (C–C motif) ligand (*Ccl*) and Chemokine (C-X-C motif) ligand (*Cxcl*) gene expression levels across different cell clusters and then compared selected candidates between sham and T + E2 animals (Fig. 4C,D). This screen

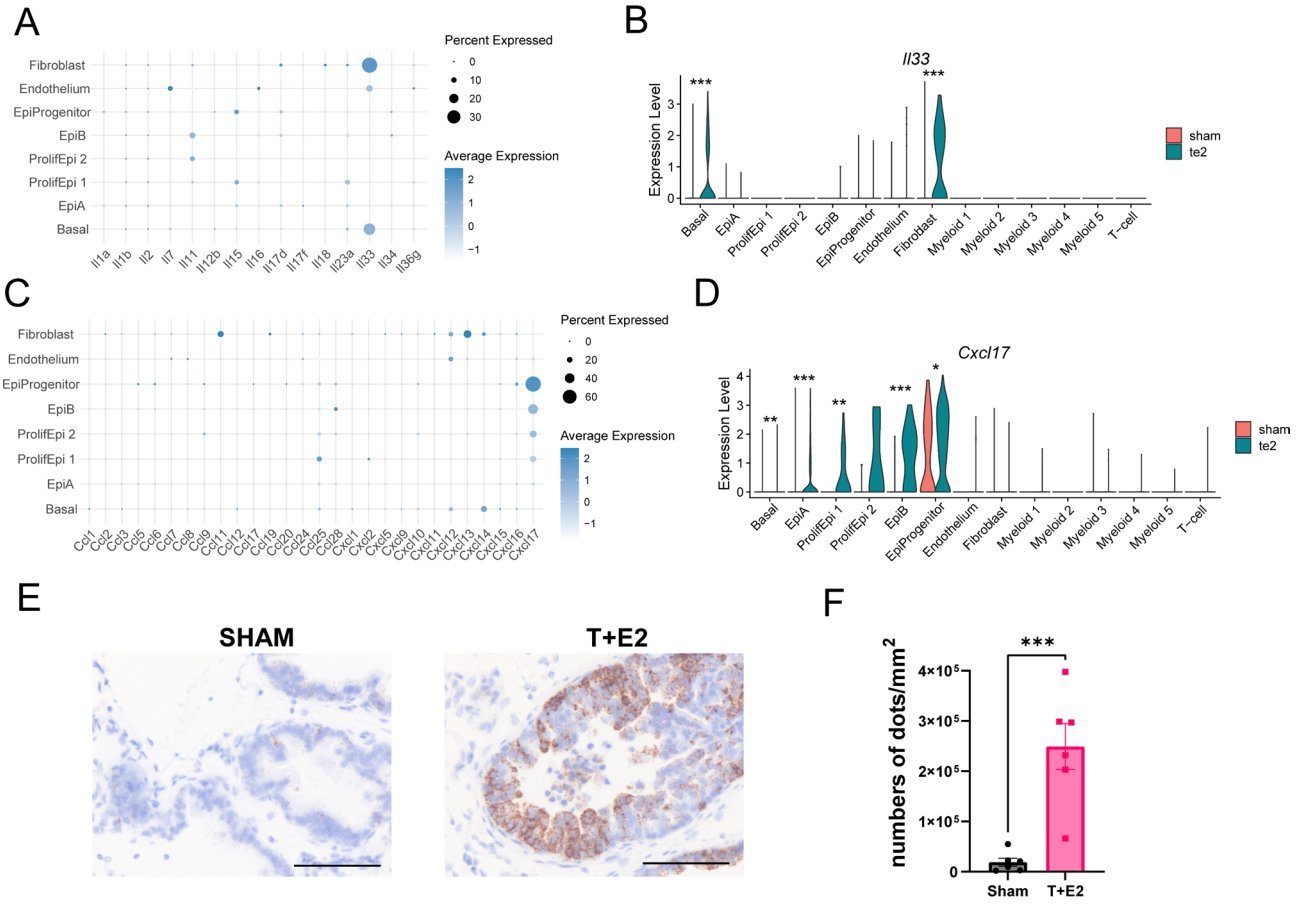

Fig. 4. Steroid hormone imbalance stimulates *Cxcl17* expression in epithelial cells. Expression of cytokines and chemokines was further analyzed in epithelial cluster scRNA-seq data and confirmed with RNAscope. (**A**) Dot blot showing the expression of interleukines in resident prostate cells. (**B**) Violin plot demonstrating expressional changes in *Il33* in control and T + E2 ventral prostate in all cell clusters. (**C**) Dot blot showing the expression of chemokines in resident prostate cells. (**D**) Violin plot demonstrating expressional changes in *Cxcl17* in control and T + E2 ventral prostate in all cell clusters. (**E**) Spatial localization and expression of *Cxcl17* in sham and T + E2 ventral prostates with in situ hybridization. (**F**) Quantification of *Cxcl17* expression. Scale bars represent 100 µm. Significance was tested using Student`s t-test. ***$p \leq 0.001$. Error bars represent SEM.

identified *Cxcl17* as an upregulated gene in epithelial clusters (Basal $p < 0.01$, EpiA $p < 0.001$, ProlifEpi1 $p < 0.01$, EpiB $p < 0.001$, and EpiProgenitor $p < 0.05$). RNAscope determined a significant 13-fold upregulation in *Cxcl17* expression in T + E2 mice (Fig. 5E,F) and thereby confirmed the scRNA-seq results. CXCL17 is a known monocyte attractant[50] indicating that it may be the primary driver of the increase in macrophages in the tissue as well as macrophage translocation to the lumen.

Discussion

In a recent study, we found that luminal foam cells accumulated specifically in the ventral prostate lobe in both a mouse model of age-related steroid hormone imbalance and in human BPH[19]. Building on these findings, our current study explored the changing immune cell milieu, the transcriptome of luminal foam cells and identified secreted factors of resident prostate cells with the potential to drive immune cell infiltration in response to testosterone and estradiol slow-release pellets.

Multiple epithelial cell types were observed, including secretory epithelial cell types EpiA and EpiB, consistent with previous scRNA-seq analyses of healthy mouse prostates[29–31]. The representation of EpiB cells was found to be limited, corroborating earlier findings which identified these cells predominantly in the anterior, lateral, and dorsal lobes[29]. Additionally, our findings highlighted a significant increase in the representation of progenitor "urothelial" epithelial cells[29–31] as well as basal cells in response to steroid hormone imbalance (T + E2 vs. sham). Urothelial cells in the prostate are known to express various progenitor markers and have been characterized as castration-resistant/androgen-independent luminal cells that proliferate in response to androgen-induced stromal growth factors[30,51]. The analogous cell type in humans was observed to be enriched in BPH patients treated with 5-alpha-reductase inhibitors (5ARIs)[30]. Our study demonstrated that estradiol/testosterone supplementation also produces an increase in urothelial epithelial cells.

Our characterization of prostatic fibroblasts provided three subtypes. Our Fibroblast 1 cluster is identical to "Prostate fibroblast" earlier recognized by Joseph et al.[32] and showed a highly metabolically active state represented by increased monosaccharide and carbohydrate import pathways. Fibroblast 2 and 3 were mainly localized to the subepithelial region and were potentially subtypes of the "ductal fibroblasts" identified by Joseph et al.[32] Most importantly, we found the highest expression of collagen genes in Fibroblast 3 cells emphasizing that this cell type could be a driver of prostatic fibrosis in the advanced stages of this model[19]. Our future studies will confirm this hypothesis in more chronic stages of the model. Intriguingly, we identified that intraluminal tissue involutions are composed of all three fibroblast cell types. We found only one other reference to this structure, described as fibroplasia, in mice with *Vhl* and *Eaf2* deficiency. Such mice exhibit increased VEGF expression and microvascular density[52] suggesting that these factors might contribute to the formation of stromal invagination, but further experimental investigation is needed to confirm this hypothesis. Finally, the lack of smooth muscle cells in our dataset was potentially due to the digestion protocol selected (cold protease), which will be adjusted in the future to avoid the loss of this cell type.

The immune environment captured included four macrophage clusters, one dendritic cell cluster and one T-cell cluster. Based on gene expression signatures, Mac^{CD72+} were pro-inflammatory (M1), Mac^{Ear2+} were alternatively activated (M2), Mac^{Mrc1+} were resident macrophages, and Mac^{Spp1+} were foam cells. Within the resident macrophage cluster, the presence of cells expressing the classical monocyte marker *Ccr2* + suggests that these cells are subject to monocyte-mediated replenishment. Resident macrophages support tissue functionality; Mac^{Mrc1+} cells exhibited *Cd36* levels comparable to those of foam cells, indicating a potential role in lipid homeostasis. However, steroid hormone imbalance led to an increase in all macrophage subsets, except for resident macrophages, indicating the pivotal role of macrophage infiltration in this model. Mac^{CD72+} in the heart were shown to be pro-inflammatory and promote cardiac injury.[53] Cells with similar marker gene signature have been identified as interstitial macrophages that respond to LPS treatment[54] and may represent the pro-inflammatory macrophage subset we identified in an earlier study based on iNOS expression[19]. Conversely, Mac^{Ear2+} (myeloid 2) cells carried *Retnla* universal and *Ear2* monocyte-derived alternatively activated (M2) macrophage markers[36,37].

Mac^{Spp1+} cells were delineated in our prior study as intraluminal foamy macrophages in this model, setting the stage for the goal of our current study to further elucidate their characteristics[19]. We found that, *Gpnmb* and *Trem2*, recognized foam cell markers in atherosclerosis, were also present in this macrophage subset[39]. Although foam cells in atherosclerosis are known to exacerbate inflammation through their accumulation and formation of a necrotic core via programmed cell death[20] their phenotype is closer to an anti-inflammatory M2 state based on markers *Cd9*, *Ctsb*, *Fabp4*, and *Lgals3*[55–57]. Foam cells may also constitute a heterogenous population where a *Spp1* + *Trem2*– subtype undergoing endoplasmic reticulum stress, apoptosis and autophagy possesses amplified glycolytic and angiogenic activities[58]. The presence of oxidized lipids induced the expression of pro-inflammatory genes *TNF* and *IL6* in human macrophages, indicating that foam cells might initially present an M1 phenotype[59].

Our focus was on uncovering the pathological significance of foam cells in the prostate by analyzing their marker gene expression, and identified *Tgfb1*, *Vegfa*, *Cxcl16*, *Ccl6* and *Mmp12* as potential mediators. TGF-β1 is widely recognized as a key factor that promotes fibrosis and concurrently compromises the integrity of the barrier function in prostate epithelial cells[40,41]. Our scRNA-seq data revealed that foam cells exhibited the highest level of VEGF expression among all cell types in the integrated dataset. VEGF-A has been implicated in the enhancement of microvascular density within BPH nodules, signifying its contribution to the progression of BPH[44]. Previous studies have suggested that VEGF expression is regulated by testosterone and estradiol, and the withdrawal of either hormone can result in significant hypoxia and loss of vascularity[60–63]. In addition, the combination of testosterone and estradiol increased prostatic microvascular density in Sprague–Dawley rats[64]. These studies strongly indicate the steroid hormone-dependence of prostatic VEGF expression, however, it remains unclear whether the formation of foam cells led to a foam cell type-specific VEGF expression level or if steroid hormones directly modulated VEGF levels in these macrophages.

CXCL16 attracts mainly T-cells and promotes fibrosis[65,66] whereas CCL6 attracts monocytes and macrophages[43] signifying the potential role of foam cells in initiating an inflammatory response in the prostate. Moreover, MMP12 emerged as a crucial foam cell-secreted enzyme that not only facilitates macrophage migration—thereby influencing inflammatory responses—but also plays a significant role in increasing the permeability of epithelial barriers[42]. Finally, osteopontin (*Spp1*), the first foam cell-secreted factor identified in BPH by our previous study, is a pro-inflammatory, pro-fibrotic protein[19,67–69]. Osteopontin is efficiently taken up by adjacent epithelial cells, as demonstrated by immunohistochemistry, highlighting the potential impact of foam cell-derived proteins on tissue homeostasis and disease progression[19]. Such proteins, especially in areas where epithelial integrity is already compromised, possibly due to the actions of TGF-β1 or MMP12, might indeed augment disease processes. Our future studies will focus on understanding the mechanisms by which these factors contribute to disease to provide valuable insights into potential therapeutic targets for intervention.

We also explored the cytokines involved in monocyte infiltration and macrophage luminal translocation. Importantly, *Cxcl17*, a gene that encodes a secreted chemokine, showed increased levels in luminal epithelial cells in response to steroid hormone imbalance. Past studies have shown CXCL17 to act as a chemoattractant for monocytes/macrophages, exerting a comparatively weaker effect on dendritic cells[50]. The epithelial expression and potential luminal secretion of CXCL17 also align with expectations for a cytokine that could facilitate the movement of macrophages into the luminal space. Therefore, our future studies will aim to elucidate whether the observed upregulation of CXCL17 in steroid hormone imbalance, mediates macrophage mobilization and infiltration into the luminal compartment, thereby facilitating foam cell formation. Additionally, we found that *Il33* was upregulated in basal epithelium and fibroblasts. Typically, IL33 protein is not secreted and retained in the nucleus, becoming active only when released due to cell damage[70]. However, more recent findings have shown that IL33 may be secreted through the neutral sphingomyelinase 2 endosome pathway[71]. IL33 promotes the

proliferation and survival of immune cells and triggers a type 2 immune response[72,73] but, as discussed above, may only contribute to a more extensive response in the prostate following cell death, such as in inflammatory atrophy.

Within our framework, the direct influence of estradiol on macrophages is also expected to play a role. Estradiol has been shown to diminish LPS-induced NF-κB activation and IL-6 production in monocytes and macrophages[74,75]. Furthermore, it reduced monocyte adhesion through the downregulation of Rac1 GTPase activity[76]. Estradiol also promoted wound healing by inducing M2 polarization through macrophage-specific estrogen receptor alpha (ERα) signaling[77] collectively underscoring its anti-inflammatory properties. The effects of estradiol, however, exhibited sexual dimorphism; it inhibited LDL-induced lipid accumulation in macrophages derived from female subjects but did not affect those from male subjects[78]. Estradiol also diminished M2a activation in macrophages from males[79]. However, considering the complexity of an in vivo system, the direct effects of estradiol might be inferior to other paracrine factors on macrophages; the direct action of estradiol, for example, should inhibit foam cell formation by decreasing lipid accumulation in macrophages, as previously shown[80], which contrasts with our observations in the male steroid hormone imbalance model. Another possibility is that local estrogen levels were highly variable in the tissue microenvironment, especially, when we compare tissue vs. intraluminal areas. Our future studies will aim to test these hypotheses to provide a molecular mechanism of how steroid hormone imbalance drives foam cell formation in the prostate.

Overall, the obtained transcriptomics characterization, especially as it relates to foam cells, is highly relevant to human disease. We have previously confirmed that the accumulation of lipid-laden macrophages in the lumen also occured in BPH prostates[23]. The human version of some of the identified foam cell genes, *FABP4*, *GPNMB* and *SPP1*, were also markers of human atherosclerotic foam cells[58]. Therefore, our study will likely lead to tools for identifying human prostatic foam cells but also reports on the pathological factors (*VEGF*, *SPP1*, *TGFB1*, *MMP12*) that may drive disease progression. Our future studies will decipher the analogies in the pathological role of specific macrophage subsets between this mouse model and BPH.

A weakness of our study is that the sham control samples had fewer genes identified per cell, which may have been due to the cold protease digestion methodology, but what was kept consistent between the two groups. To address this, we have confirmed all major findings with a secondary method of in situ hybridization or immunohistochemistry. Current work in the lab is ongoing to optimize digestion strategies and to increase sample number to further identify differences in cell populations within the steroid hormone model.

In conclusion, we have characterized changes in prostate cell heterogeneity in the mouse steroid hormone imbalance model in the ventral prostate. We found increases in progenitor and basal epithelial cells as well as in three subsets of macrophages. Most importantly, we have identified important secreted factors specific for luminal foam cells as well as identified CXCL17 as a candidate for directing macrophage trafficking in the prostate. Our future studies will mechanistically decipher the role of these newly identified molecular drivers, especially how luminally-secreted factors drive disease pathogenesis in BPH.

Data availability

Expression data is accessible through GEO Series accession number GSE263790.

Received: 23 May 2024; Accepted: 26 August 2024
Published online: 09 September 2024

References

1. Roehrborn, C. G. Benign prostatic hyperplasia: An overview. *Rev. Urol.* **7**(Suppl 9), S3–S14 (2005).
2. Devlin, C. M., Simms, M. S. & Maitland, N. J. Benign prostatic hyperplasia—What do we know?. *BJU Int.* **127**, 389–399. https://doi.org/10.1111/bju.15229 (2021).
3. McVary, K. T. BPH: Epidemiology and comorbidities. *Am. J. Manag. Care* **12**, S122-128 (2006).
4. Hollingsworth, J. M. & Wei, J. T. Economic impact of surgical intervention in the treatment of benign prostatic hyperplasia. *Rev. Urol.* **8**(Suppl 3), S9–S15 (2006).
5. Lepor, H. Pathophysiology of lower urinary tract symptoms in the aging male population. *Rev. Urol.* **7**(Suppl 7), S3–S11 (2005).
6. Stroup, S. P., Palazzi-Churas, K., Kopp, R. P. & Parsons, J. K. Trends in adverse events of benign prostatic hyperplasia (BPH) in the USA, 1998 to 2008. *BJU Int.* **109**, 84–87. https://doi.org/10.1111/j.1464-410X.2011.10250.x (2012).
7. Vuichoud, C. & Loughlin, K. R. Benign prostatic hyperplasia: Epidemiology, economics and evaluation. *Can. J. Urol.* **22**(Suppl 1), 1–6 (2015).
8. Strand, D. W., Aaron, L., Henry, G., Franco, O. E. & Hayward, S. W. Isolation and analysis of discreet human prostate cellular populations. *Differentiation* **91**, 139–151. https://doi.org/10.1016/j.diff.2015.10.013 (2016).
9. Vickman, R. E. *et al.* TNF is a potential therapeutic target to suppress prostatic inflammation and hyperplasia in autoimmune disease. *Nat. Commun.* **13**, 2133. https://doi.org/10.1038/s41467-022-29719-1 (2022).
10. Rodriguez-Nieves, J. A. & Macoska, J. A. Prostatic fibrosis, lower urinary tract symptoms, and BPH. *Nat. Rev. Urol.* **10**, 546–550. https://doi.org/10.1038/nrurol.2013.149 (2013).
11. Macoska, J. A., Uchtmann, K. S., Leverson, G. E., McVary, K. T. & Ricke, W. A. Prostate transition zone fibrosis is associated with clinical progression in the MTOPS study. *J. Urol.* **202**, 1240–1247. https://doi.org/10.1097/JU.0000000000000385 (2019).
12. Vital, P., Castro, P., Tsang, S. & Ittmann, M. The senescence-associated secretory phenotype promotes benign prostatic hyperplasia. *Am. J. Pathol.* **184**, 721–731. https://doi.org/10.1016/j.ajpath.2013.11.015 (2014).
13. Begley, L., Monteleon, C., Shah, R. B., Macdonald, J. W. & Macoska, J. A. CXCL12 overexpression and secretion by aging fibroblasts enhance human prostate epithelial proliferation in vitro. *Aging Cell* **4**, 291–298. https://doi.org/10.1111/j.1474-9726.2005.00173.x (2005).
14. Castro, P., Giri, D., Lamb, D. & Ittmann, M. Cellular senescence in the pathogenesis of benign prostatic hyperplasia. *Prostate* **55**, 30–38. https://doi.org/10.1002/pros.10204 (2003).
15. Gharaee-Kermani, M. *et al.* Obesity-induced diabetes and lower urinary tract fibrosis promote urinary voiding dysfunction in a mouse model. *Prostate* **73**, 1123–1133. https://doi.org/10.1002/pros.22662 (2013).
16. Nicholson, T. M. & Ricke, W. A. Androgens and estrogens in benign prostatic hyperplasia: Past, present and future. *Differentiation* **82**, 184–199. https://doi.org/10.1016/j.diff.2011.04.006 (2011).

17. Shibata, Y. et al. Changes in the endocrine environment of the human prostate transition zone with aging: simultaneous quantitative analysis of prostatic sex steroids and comparison with human prostatic histological composition. *Prostate.* **42**, 45–55 (2000). https://doi.org/10.1002/(sici)1097-0045(20000101)42:1<45::aid-pros6>3.0.co;2-w.
18. Nicholson, T. M. *et al.* Testosterone and 17beta-estradiol induce glandular prostatic growth, bladder outlet obstruction, and voiding dysfunction in male mice. *Endocrinology* **153**, 5556–5565. https://doi.org/10.1210/en.2012-1522 (2012).
19. Popovics, P. *et al.* Steroid hormone imbalance drives macrophage infiltration and Spp1/osteopontin(+) foam cell differentiation in the prostate. *J. Pathol.* **260**, 177–189. https://doi.org/10.1002/path.6074 (2023).
20. Gui, Y., Zheng, H. & Cao, R. Y. Foam cells in atherosclerosis: Novel insights into its origins, consequences, and molecular mechanisms. *Front. Cardiovasc. Med.* **9**, 845942. https://doi.org/10.3389/fcvm.2022.845942 (2022).
21. Brophy, M. L. *et al.* Eating the dead to keep atherosclerosis at bay. *Front. Cardiovasc. Med.* **4**, 2. https://doi.org/10.3389/fcvm.2017.00002 (2017).
22. Hou, X. *et al.* Lipid uptake by alveolar macrophages drives fibrotic responses to silica dust. *Sci. Rep.* **9**, 399. https://doi.org/10.1038/s41598-018-36875-2 (2019).
23. Popovics, P. *et al.* Steroid hormone imbalance drives macrophage infiltration and Spp1/osteopontin(+) foam cell differentiation in the prostate. *J. Pathol.* https://doi.org/10.1002/path.6074 (2023).
24. Martin, F. J. *et al.* Ensembl 2023. *Nucleic Acids Res.* **51**, D933–D941. https://doi.org/10.1093/nar/gkac958 (2023).
25. Sullivan, D. K. *et al.* Kallisto, bustools, and kb-python for quantifying bulk, single-cell, and single-nucleus RNA-seq. *bioRxiv* https://doi.org/10.1101/2023.11.21.568164 (2024).
26. Hao, Y. *et al.* Integrated analysis of multimodal single-cell data. *Cell* **184**, 3573-3587 e3529. https://doi.org/10.1016/j.cell.2021.04.048 (2021).
27. Hao, Y. *et al.* Dictionary learning for integrative, multimodal and scalable single-cell analysis. *Nat. Biotechnol.* **42**, 293–304. https://doi.org/10.1038/s41587-023-01767-y (2024).
28. Wu, T. *et al.* clusterProfiler 4.0: A universal enrichment tool for interpreting omics data. *Innovation (Camb).* **2**, 100141. https://doi.org/10.1016/j.xinn.2021.100141 (2021).
29. Guo, W. *et al.* Single-cell transcriptomics identifies a distinct luminal progenitor cell type in distal prostate invagination tips. *Nat. Genet.* **52**, 908–918. https://doi.org/10.1038/s41588-020-0642-1 (2020).
30. Joseph, D. B. *et al.* Urethral luminal epithelia are castration-insensitive cells of the proximal prostate. *Prostate* **80**, 872–884. https://doi.org/10.1002/pros.24020 (2020).
31. Crowley, L. *et al.* A single-cell atlas of the mouse and human prostate reveals heterogeneity and conservation of epithelial progenitors. *Elife* https://doi.org/10.7554/eLife.59465 (2020).
32. Joseph, D. B. *et al.* Single-cell analysis of mouse and human prostate reveals novel fibroblasts with specialized distribution and microenvironment interactions. *J. Pathol.* **255**, 141–154. https://doi.org/10.1002/path.5751 (2021).
33. Liu, Y. *et al.* Single-cell profiling reveals divergent, globally patterned immune responses in murine skin inflammation. *iScience* **23**, 101582. https://doi.org/10.1016/j.isci.2020.101582 (2020).
34. Meghraoui-Kheddar, A., Barthelemy, S., Boissonnas, A. & Combadiere, C. Revising CX3CR1 expression on murine classical and non-classical monocytes. *Front. Immunol.* **11**, 1117. https://doi.org/10.3389/fimmu.2020.01117 (2020).
35. Geissmann, F., Jung, S. & Littman, D. R. Blood monocytes consist of two principal subsets with distinct migratory properties. *Immunity* **19**, 71–82. https://doi.org/10.1016/s1074-7613(03)00174-2 (2003).
36. Harasymowicz, N. S. *et al.* Single-cell RNA sequencing reveals the induction of novel myeloid and myeloid-associated cell populations in visceral fat with long-term obesity. *FASEB J.* **35**, e21417. https://doi.org/10.1096/fj.202001970R (2021).
37. Gundra, U. M. *et al.* Alternatively activated macrophages derived from monocytes and tissue macrophages are phenotypically and functionally distinct. *Blood* **123**, e110-122. https://doi.org/10.1182/blood-2013-08-520619 (2014).
38. Ma, J. *et al.* Single-cell RNA-Seq analysis of diabetic wound macrophages in STZ-induced mice. *J. Cell Commun. Signal* **17**, 103–120. https://doi.org/10.1007/s12079-022-00707-w (2023).
39. Zernecke, A. *et al.* Meta-analysis of leukocyte diversity in atherosclerotic mouse aortas. *Circ. Res.* **127**, 402–426. https://doi.org/10.1161/CIRCRESAHA.120.316903 (2020).
40. Li, F. *et al.* Transforming growth factor beta 1 impairs benign prostatic luminal epithelial cell monolayer barrier function. *Am. J. Clin. Exp. Urol.* **8**, 9–17 (2020).
41. Gharaee-Kermani, M. *et al.* CXC-type chemokines promote myofibroblast phenoconversion and prostatic fibrosis. *PLoS One* **7**, e49278. https://doi.org/10.1371/journal.pone.0049278 (2012).
42. Nighot, M. *et al.* Matrix metalloproteinase MMP-12 promotes macrophage transmigration across intestinal epithelial tight junctions and increases severity of experimental colitis. *J. Crohns Colitis* **15**, 1751–1765. https://doi.org/10.1093/ecco-jcc/jjab064 (2021).
43. Feng, X. *et al.* CCL6 promotes M2 polarization and inhibits macrophage autophagy by activating PI3-kinase/Akt signalling pathway during skin wound healing. *Exp. Dermatol.* **32**, 403–412. https://doi.org/10.1111/exd.14718 (2023).
44. Deering, R. E., Bigler, S. A., Brown, M. & Brawer, M. K. Microvascularity in benign prostatic hyperplasia. *Prostate* **26**, 111–115. https://doi.org/10.1002/pros.2990260302 (1995).
45. Abel, S. *et al.* The transmembrane CXC-chemokine ligand 16 is induced by IFN-gamma and TNF-alpha and shed by the activity of the disintegrin-like metalloproteinase ADAM10. *J. Immunol.* **172**, 6362–6372. https://doi.org/10.4049/jimmunol.172.10.6362 (2004).
46. Pepino, M. Y., Kuda, O., Samovski, D. & Abumrad, N. A. Structure-function of CD36 and importance of fatty acid signal transduction in fat metabolism. *Annu. Rev. Nutr.* **34**, 281–303. https://doi.org/10.1146/annurev-nutr-071812-161220 (2014).
47. Furuhashi, M. & Hotamisligil, G. S. Fatty acid-binding proteins: Role in metabolic diseases and potential as drug targets. *Nat. Rev. Drug Discov.* **7**, 489–503. https://doi.org/10.1038/nrd2589 (2008).
48. Castano, D. *et al.* Lipid efflux mechanisms, relation to disease and potential therapeutic aspects. *Adv. Drug Deliv. Rev.* **159**, 54–93. https://doi.org/10.1016/j.addr.2020.04.013 (2020).
49. Liew, F. Y., Girard, J. P. & Turnquist, H. R. Interleukin-33 in health and disease. *Nat. Rev. Immunol.* **16**, 676–689. https://doi.org/10.1038/nri.2016.95 (2016).
50. Hiraoka, N. *et al.* CXCL17 and ICAM2 are associated with a potential anti-tumor immune response in early intraepithelial stages of human pancreatic carcinogenesis. *Gastroenterology* **140**, 310–321. https://doi.org/10.1053/j.gastro.2010.10.009 (2011).
51. Karthaus, W. R. *et al.* Regenerative potential of prostate luminal cells revealed by single-cell analysis. *Science* **368**, 497–505. https://doi.org/10.1126/science.aay0267 (2020).
52. Pascal, L. E. *et al.* EAF2 loss enhances angiogenic effects of Von Hippel-Lindau heterozygosity on the murine liver and prostate. *Angiogenesis* **14**, 331–343. https://doi.org/10.1007/s10456-011-9217-1 (2011).
53. Ni, S. H. *et al.* Single-cell transcriptomic analyses of cardiac immune cells reveal that Rel-driven CD72-positive macrophages induce cardiomyocyte injury. *Cardiovasc. Res.* **118**, 1303–1320. https://doi.org/10.1093/cvr/cvab193 (2022).
54. Lyras, E. M. *et al.* Tongue immune compartment analysis reveals spatial macrophage heterogeneity. *Elife* https://doi.org/10.7554/eLife.77490 (2022).
55. Lin, J. D. *et al.* Single-cell analysis of fate-mapped macrophages reveals heterogeneity, including stem-like properties, during atherosclerosis progression and regression. *JCI Insight* https://doi.org/10.1172/jci.insight.124574 (2019).
56. Kim, K. *et al.* Transcriptome analysis reveals nonfoamy rather than foamy plaque macrophages are proinflammatory in atherosclerotic murine models. *Circ. Res.* **123**, 1127–1142. https://doi.org/10.1161/CIRCRESAHA.118.312804 (2018).

57. McArdle, S. *et al.* Migratory and dancing macrophage subsets in atherosclerotic lesions. *Circ. Res.* **125**, 1038–1051. https://doi.org/10.1161/CIRCRESAHA.119.315175 (2019).
58. Xiong, J. *et al.* Bulk and single-cell characterisation of the immune heterogeneity of atherosclerosis identifies novel targets for immunotherapy. *BMC Biol.* **21**, 46. https://doi.org/10.1186/s12915-023-01540-2 (2023).
59. Schwarz, A., Bonaterra, G. A., Schwarzbach, H. & Kinscherf, R. Oxidized LDL-induced JAB1 influences NF-kappaB independent inflammatory signaling in human macrophages during foam cell formation. *J. Biomed. Sci.* **24**, 12. https://doi.org/10.1186/s12929-017-0320-5 (2017).
60. Aberdeen, G. W., Babischkin, J. S., Pepe, G. J. & Albrecht, E. D. Estrogen stimulates fetal vascular endothelial growth factor expression and microvascularization. *J. Endocrinol.* https://doi.org/10.1530/JOE-23-0364 (2024).
61. Buttyan, R., Ghafar, M. A. & Shabsigh, A. The effects of androgen deprivation on the prostate gland: Cell death mediated by vascular regression. *Curr. Opin. Urol.* **10**, 415–420. https://doi.org/10.1097/00042307-200009000-00009 (2000).
62. Stewart, R. J., Panigrahy, D., Flynn, E. & Folkman, J. Vascular endothelial growth factor expression and tumor angiogenesis are regulated by androgens in hormone responsive human prostate carcinoma: Evidence for androgen dependent destabilization of vascular endothelial growth factor transcripts. *J. Urol.* **165**, 688–693. https://doi.org/10.1097/00005392-200102000-00095 (2001).
63. Wang, G. M., Kovalenko, B., Wilson, E. L. & Moscatelli, D. Vascular density is highest in the proximal region of the mouse prostate. *Prostate* **67**, 968–975. https://doi.org/10.1002/pros.20582 (2007).
64. Wang, B. *et al.* The relationship between prostatic microvessel density and different concentrations of oestrogen/androgen in Sprague–Dawley rats. *Eur. J. Med. Res.* **27**, 87. https://doi.org/10.1186/s40001-022-00719-7 (2022).
65. Matloubian, M., David, A., Engel, S., Ryan, J. E. & Cyster, J. G. A transmembrane CXC chemokine is a ligand for HIV-coreceptor Bonzo. *Nat. Immunol.* **1**, 298–304. https://doi.org/10.1038/79738 (2000).
66. Liang, H. *et al.* CXCL16 deficiency attenuates renal injury and fibrosis in salt-sensitive hypertension. *Sci. Rep.* **6**, 28715. https://doi.org/10.1038/srep28715 (2016).
67. Popovics, P. *et al.* Osteopontin deficiency ameliorates prostatic fibrosis and inflammation. *Int. J. Mol. Sci.* https://doi.org/10.3390/ijms222212461 (2021).
68. Silver, S. V. & Popovics, P. The multifaceted role of osteopontin in prostate pathologies. *Biomedicines* https://doi.org/10.3390/biomedicines11112895 (2023).
69. Popovics, P. *et al.* Prostatic osteopontin expression is associated with symptomatic benign prostatic hyperplasia. *Prostate* **80**, 731–741. https://doi.org/10.1002/pros.23986 (2020).
70. Cayrol, C. & Girard, J. P. IL-33: An alarmin cytokine with crucial roles in innate immunity, inflammation and allergy. *Curr. Opin. Immunol.* **31**, 31–37. https://doi.org/10.1016/j.coi.2014.09.004 (2014).
71. Katz-Kiriakos, E. *et al.* Epithelial IL-33 appropriates exosome trafficking for secretion in chronic airway disease. *JCI Insight* https://doi.org/10.1172/jci.insight.136166 (2021).
72. Lott, J. M., Sumpter, T. L. & Turnquist, H. R. New dog and new tricks: Evolving roles for IL-33 in type 2 immunity. *J. Leukoc. Biol.* **97**, 1037–1048. https://doi.org/10.1189/jlb.3RI1214-595R (2015).
73. Molofsky, A. B., Savage, A. K. & Locksley, R. M. Interleukin-33 in tissue homeostasis, injury, and inflammation. *Immunity* **42**, 1005–1019. https://doi.org/10.1016/j.immuni.2015.06.006 (2015).
74. Pelekanou, V. *et al.* Estrogen anti-inflammatory activity on human monocytes is mediated through cross-talk between estrogen receptor ERalpha36 and GPR30/GPER1. *J. Leukoc. Biol.* **99**, 333–347. https://doi.org/10.1189/jlb.3A0914-430RR (2016).
75. Okamoto, M., Suzuki, T., Mizukami, Y. & Ikeda, T. The membrane-type estrogen receptor G-protein-coupled estrogen receptor suppresses lipopolysaccharide-induced interleukin 6 via inhibition of nuclear factor-kappa B pathway in murine macrophage cells. *Anim. Sci. J.* **88**, 1870–1879. https://doi.org/10.1111/asj.12868 (2017).
76. Friedrich, E. B., Clever, Y. P., Wassmann, S., Hess, C. & Nickenig, G. 17Beta-estradiol inhibits monocyte adhesion via down-regulation of Rac1 GTPase. *J. Mol. Cell Cardiol.* **40**, 87–95. https://doi.org/10.1016/j.yjmcc.2005.10.007 (2006).
77. Campbell, L. *et al.* Estrogen receptor-alpha promotes alternative macrophage activation during cutaneous repair. *J. Investig. Dermatol.* **134**, 2447–2457. https://doi.org/10.1038/jid.2014.175 (2014).
78. McCrohon, J. A., Nakhla, S., Jessup, W., Stanley, K. K. & Celermajer, D. S. Estrogen and progesterone reduce lipid accumulation in human monocyte-derived macrophages: A sex-specific effect. *Circulation* **100**, 2319–2325. https://doi.org/10.1161/01.cir.100.23.2319 (1999).
79. Ray, J. L. *et al.* Estrogen contributes to sex differences in M2a macrophages during multi-walled carbon nanotube-induced respiratory inflammation. *FASEB J.* **38**, e23350. https://doi.org/10.1096/fj.202301571RR (2024).
80. Xie, F. *et al.* Estrogen mediates an atherosclerotic-protective action via estrogen receptor Alpha/SREBP-1 signaling. *Front. Cardiovasc. Med.* **9**, 895916. https://doi.org/10.3389/fcvm.2022.895916 (2022).

Acknowledgements

We thank Xin (Cindy) Guo, Chunghwan Ro, Daniel McWilliams, Mary Ann Clements and Dita Julianingsih for experimental assistance and advice. This research was funded by grants from the National Institutes of Health (K01 DK127150 to P.P and 1 U2C CA271894-01 to OJS), financial support from the Hampton Roads Biomedical Research Consortium and a start-up fund from the Eastern Virginia Medical School (to P.P.). The authors thank the EVMS Histology Services Lab for providing its services.

Author contributions

P.P. and N.S.A. conceptualized the study. P.P. and O.J.S. acquired funding. P.P. and N.S.A. developed the methodology. S.V.S., P.P. and K.J.T. performed the experiments and conducted the formal analysis. P.P. and S.V.S. visualized the data. P.P. wrote the manuscript and R.E.V., N.A.L., N.S.A. and O.J.S. conducted manuscript review and editing. All authors have read and agreed to the published version of the manuscript.

Competing interests

The authors declare no competing interests.

Additional information

Supplementary Information The online version contains supplementary material available at https://doi.org/10.1038/s41598-024-71137-4.

Correspondence and requests for materials should be addressed to P.P.